ACS APPLIED ENERGY MATERIALS

www.acsaem.org Article

Fluorinated Zinc and Copper Phthalocyanines as Efficient Third Components in Ternary Bulk Heterojunction Solar Cells

Alfonsina Abat Amelenan Torimtubun, Jorge Follana-Berná, José G. Sánchez, Josep Pallarès,* Ángela Sastre-Santos,* and Lluis F. Marsal*

Cite This: *ACS Appl. Energy Mater.* 2021, 4, 5201−5211 Read Online

ACCESS | Metrics & More | Article Recommendations | Supporting Information

ABSTRACT: Fluorinated zinc and copper metallophthalocyanines $MPcF_{48}$ are synthesized and incorporated as third component small molecules in ternary organic solar cells (TOSCs). To enable the high performance of TOSCs, maximizing short-circuit current density (J_{SC}) is crucial. Ternary bulk heterojunction blends, consisting of a polymer donor PTB7-Th, fullerene acceptors $PC_{70}BM$, and a third component $MPcF_{48}$, are formulated to fabricate TOSCs with a device architecture of ITO/PFN/active layer/V_2O_5/Ag. Employing copper as metal atom substitution in the third component of TOSCs enhances J_{SC} as a result of complementary absorption spectra in the near-infrared region. In combination with J_{SC} enhancement, suppressed charge recombination, improved exciton dissociation and charge carrier collection efficiency, and better morphology lead to a slightly improved fill factor (FF), resulting in a 7% enhancement of PCE than those of binary OSCs. In addition to the increased PCE, the photostability of TOSCs has also been improved by the appropriate addition of $CuPcF_{48}$. Detailed studies imply that metal atom substitution in phthalocyanines is an effective way to improve J_{SC}, FF, and thus the performance and photostability of TOSCs.

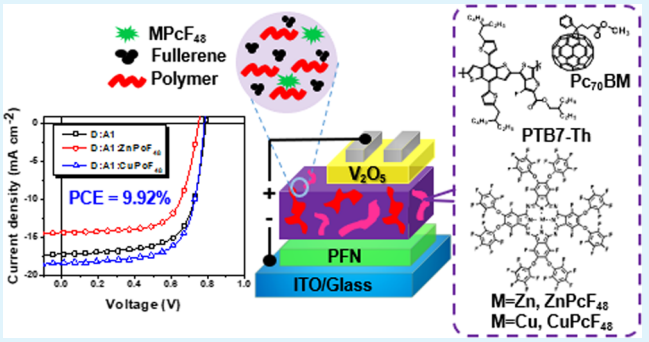

KEYWORDS: *fluorinated phthalocyanines, third component, ternary organic solar cells, bulk heterojunction, non-fullerene acceptors*

1. INTRODUCTION

Bulk heterojunction organic solar cells (OSCs) featuring properties of low cost, light-weight, solution-processed, large area, semitransparent, and flexible substrates have attracted great interest for decades.[1−6] OSCs are typically composed of an active layer consisting of electron donor (D) and electron acceptor (A) materials in the blends of single-junction OSCs or tandem cells.[7−10] However, due to low charge carrier mobility, limited spectral absorption, and high thermal loss in organic materials, the tandem cell strategy is preferred as an effective way to address these issues.[11,12] Tandem cells can suppress the thickness constraint due to the low mobility of organic materials in a single-junction cell, providing a wide and efficient optical absorption spectrum.[13] Meanwhile, thermalization losses in a single-junction cell can also be avoided thanks to the tunability band structure of the active organic materials in tandem cells.[14] Nevertheless, the complex fabrication process and high upfront cost limit the practical application of tandem cells.[15] In recent years, ternary organic solar cells (TOSCs) have been proved to be one of the most promising methods to improve device performance by adding a third component into a binary system, resulting in a single three-component photoactive layer.[16−18] TOSCs could combine each merit of binary and tandem solar cells to extend light absorption, simplify device fabrication, and increase device efficiency in a single-junction device.[16,19−21]

In a ternary blend, the addition of a third component (secondary donor D_2 or secondary acceptor A_2) provides broadened light harvesting, optimizes the film morphology, and facilitates better charge transport and exciton dissociation.[22−24] The dominant fullerene derivatives have been widely used in OSCs as a primary electron acceptor (A_1) or A_2. However, fullerene acceptors show weak light absorption, difficult energetic tunability, and thermal instability.[21,25] Recently, non-fullerene acceptors (NFAs) have been synthesized to overcome the disadvantages of FAs. The rapid progress of highly efficient NFA materials has offered a new opportunity for studying ternary OSCs due to the great tunability of chemical structures, optical and electronic properties of NFAs, and their ability to phase separate into nanoscopic domains in blended thin films.[26−31]

Received: March 12, 2021
Accepted: April 29, 2021
Published: May 12, 2021

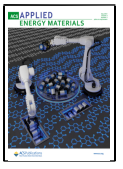

Scheme 1. Synthetic Route of $ZnPcF_{48}$ and $CuPcF_{48}$

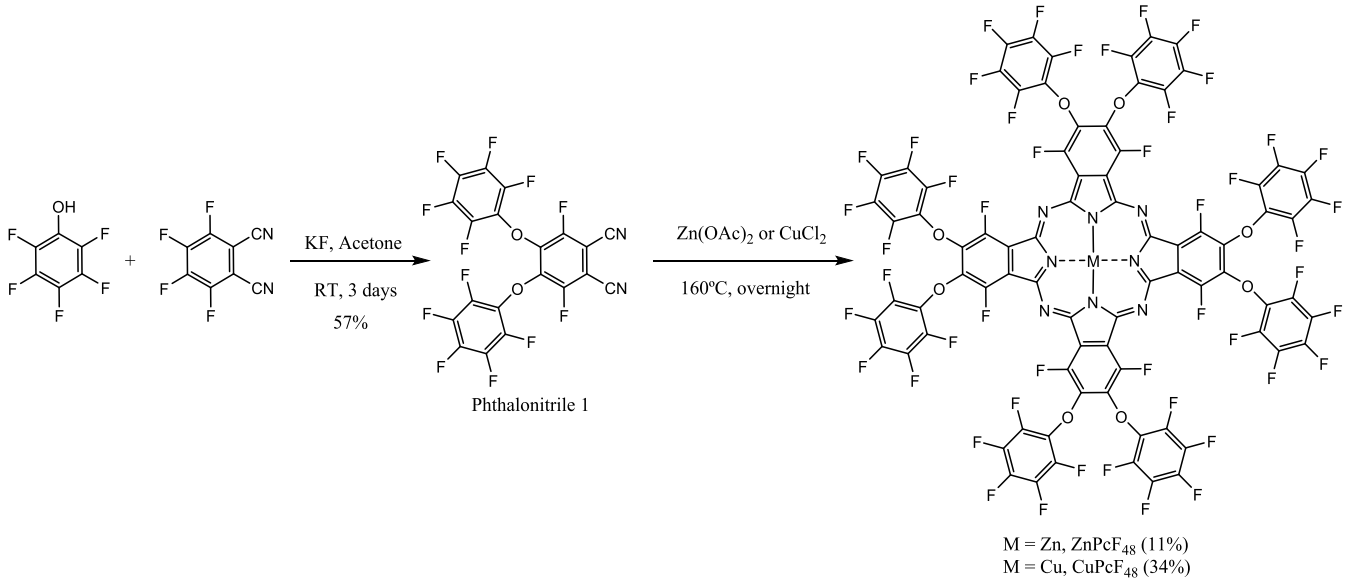

Different small molecules from phthalocyanine (Pc) derivatives have been described to provide alternative photovoltaic semiconductor materials for OSC applications.[32−35] Pcs play an important role as NFAs due to their high molar extinction coefficients, stability, and the highest occupied molecular orbital (HOMO)/lowest unoccupied molecular orbital (LUMO) energy levels complementary with the energy levels of the other two components.[36,37] However, Pcs have poor solubility in organic solvents and most of the Pcs used to date in ternary solar cells have been SiPcs thanks to the functionalization of the axial positions that avoid aggregation processes.[38−42] Due to this problem, to date, not too many Pcs have been incorporated in ternary solar cells. Different studies have been performed using CuPc[43] and ZnPc[44] as third components and in all of the cases resulted in an efficiency improvement compared to its two-component counterpart. In all these studies, Pcs act as an efficient transporter between a fullerene derivative and a polymer. For this reason, a deeper study should be done studying the influence of the substituents and the metal of the Pcs on the PV performance. In this work, we have prepared two new zinc and copper phthalocyanines substituted with electronegative fluorine atoms in benzene rings to enhance their solubility and their electron acceptor capability. Hence, $ZnPcF_{48}$ and $CuPcF_{48}$ (Scheme 1) have been synthesized and incorporated into the ternary system based on PTB7-Th:PC70BM (Figure 1) to understand their influence on the OSC device performance.

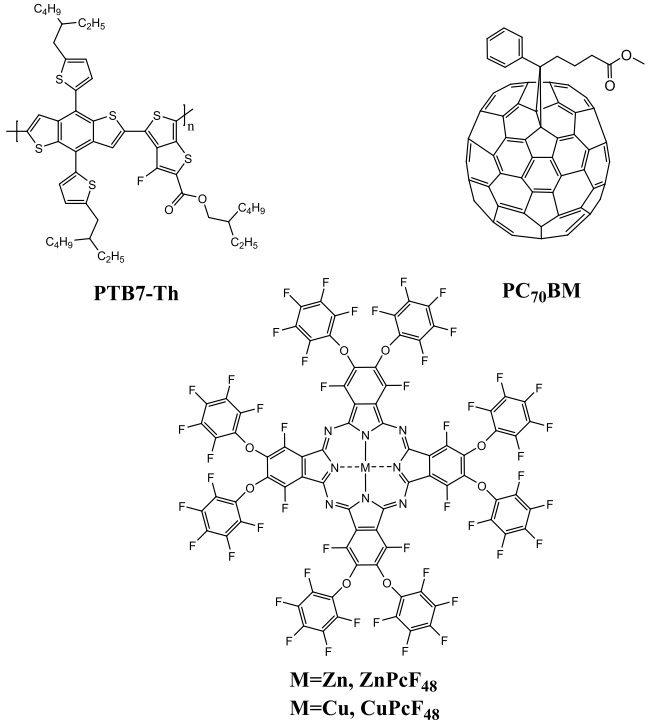

Figure 1. Chemical structures of PTB7-Th, $PC_{70}BM$, $ZnPcF_{48}$, and $CuPcF_{48}$ in ternary bulk heterojunction solar cells.

2. RESULTS AND DISCUSSION

2.1. Synthesis and Materials Properties. The synthesis of $ZnPcF_{48}$ and $CuPcF_{48}$ was accomplished by statistical cyclotetramerization of 3,6-difluoro-4,5-bis-(pentafluorophenoxy)phthalonitrile **1** using $Zn(OAc)_2$ or $CuCl_2$ as a template, respectively (Scheme 1). Phthalonitrile **1** was synthesized by nucleophilic aromatic substitution of pentafluorophenol to tetrafluorophthalonitrile and characterized by FT-IR, ^{13}C NMR, and MALDI-TOF-MS. The ^{13}C NMR spectrum was recorded without fluoride decoupling and showed several multiplets due to the coupling of ^{13}C with ^{19}F. The ^{13}C signal assignments of phthalonitrile **1** were performed by a comparative study between pentafluorophenol and tetrafluorophthalonitrile ^{13}C NMR spectra (see Figures S1 and S2).

Just like phthalonitrile **1**, $ZnPcF_{48}$ was not possible to characterize using ^{1}H NMR because of the absence of proton signals but it was characterized using ^{19}F NMR, ^{13}C NMR, and 2D NMR experiments using THF-d_8 as solvent. The ^{19}F NMR spectrum shows four different signals, and their assignment was made thanks to different multiplicities and the 2D experiment (see Figures S3 and S4). The ^{13}C NMR of $ZnPcF_{48}$ was recorded with and without fluoride decoupling, as shown in Figures S5 and S6, respectively. The carbons most affected by

https://doi.org/10.1021/acsaem.1c00734
ACS Appl. Energy Mater. 2021, 4, 5201−5211

the formation of the phthalocyanine ring are A and H, which appear more deshielded than in the case of phthalonitrile **1** (see Figure S7). The remaining carbons are not as so affected. The existence of fluorine atoms in the nonperipheral positions of the phthalocyanine ring is also demonstrated by signal B in the ^{13}C NMR experiment with fluoride coupling (see Figure S6). This signal appears as a doublet of doublets with coupling constants of 4 and 266 Hz, being the latter characteristic of $^{13}C-^{19}F$ couplings. In the case of $CuPcF_{48}$, due to the paramagnetic character of copper, this it was not possible to characterize by NMR experiments. Both phthalocyanines were further characterized by FT-IR, HR-MALDI-TOF, and UV−vis experiments. The FT-IR for both phthalocyanines shows the absence of the characteristic peak of C≡N around 2200 cm^{-1}, which appears in the FT-IR of phthalonitrile **1** (see Figures S8−S10). The mass experiments show the expected molecular peaks with an isotopic distribution that exactly matched the simulated isotopic patterns (see Figures S11−S13). The UV−vis spectra of the individual thin film and the $CHCl_3$ solution of PTB7-Th, $ZnPcF_{48}$, $CuPcF_{48}$, and $PC_{70}BM$ are shown in Figure 2a. In solution, $ZnPcF_{48}$ and $CuPcF_{48}$

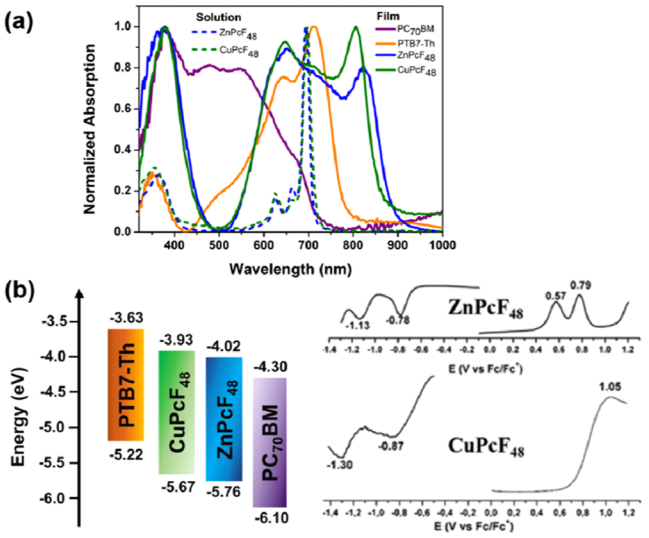

Figure 2. (a) Normalized UV−vis spectra of individual solutions (dashed lines) and thin films (solid lines) and (b) diagram representation of the estimated energy levels for PTB7-Th, $CuPcF_{48}$, $ZnPcF_{48}$, and $PC_{70}BM$ (left), calculated from differential pulse voltammetry in DCM ($ZnPcF_{48}$) and THF ($CuPcF_{48}$) using 0.1 M $TBAPF_6$ as supporting electrolyte (right).

exhibit the Soret band around 360 nm and the Q band around 694 nm, which are the characteristics of nonaggregated phthalocyanines. Compared with solution absorption spectra, $ZnPcF_{48}$ and $CuPcF_{48}$ films show a broader absorption range and, respectively, perform a red shift to the near-IR absorption spectra of 822 and 806 nm, which suggests the presence of ordered *J*-aggregations in the film.[45] Besides the near-IR absorption peak, other strong absorption peaks of $ZnPcF_{48}$ and $CuPcF_{48}$ films appear at visible ranges (378 and 652 and 382 and 648 nm), which is complementary to both PTB7-Th and $PC_{70}BM$. The complementary absorption should be beneficial to aid the photon harvesting efficiency, resulting in high short-circuit current density (J_{SC}), and further improve the efficiency of ternary devices. The complementary absorption spectra of the binary and ternary thin films are displayed in Figures S14 and S15.

Due to the $\pi-\pi$ stacking of the molecules in the solution, the oxidation and reduction potentials were not able to measure by cyclic voltammetry. These values were obtained from differential pulse voltammetry (DPV) in DCM and dry THF as solvent, for $ZnPcF_{48}$ and $CuPcF_{48}$, respectively, containing 0.1 M $TBAPF_6$ as the supporting electrolyte. As shown in Figure 2b, $ZnPcF_{48}$ has two oxidation potentials at 0.57 and 0.79 V and two reduction potentials at −0.78 and −1.13 V versus Fc/Fc^+. Meanwhile, $CuPcF_{48}$ shows one oxidation potential at 1.05 V and two reduction potentials at −0.87 and −1.30 V versus Fc/Fc^+. The estimated LUMO energy levels were calculated according to the equation $E_{LUMO} = -4.8 - E_{red}$, where E_{red} is the first reduction potential. For $ZnPcF_{48}$ and $CuPcF_{48}$, E_{LUMO} values are −4.02 and −3.93 eV, respectively. As a consequence of the difficulty to obtain the first oxidation potential of $CuPcF_{48}$, the HOMO energy levels for $ZnPcF_{48}$ and $CuPcF_{48}$ were determined, adding the absorption onset to the E_{LUMO} value. These values for $ZnPcF_{48}$ and $CuPcF_{48}$ are −5.76 and −5.67 eV, respectively, as shown in Figure 2b. The energy band gap from the absorption onset was obtained from eq 1

$$E_g\ (\text{eV}) = hx\frac{c}{\lambda} \approx \frac{1240}{\lambda} \quad (1)$$

where λ denotes the absorption edge wavelength expressed in nm, obtained from the offset wavelength derived from the low energy absorption band, as represented in Figure S16.

The HOMO and LUMO energy offsets of PTB7-Th and $PC_{70}BM$ are reduced by the addition of $ZnPcF_{48}$ and $CuPcF_{48}$ as third components in a ternary blend, which provides more pathways to enhance the charge transfer of both electrons and holes by forming a cascade energy transfer.[22,46] By using a photoluminescence instrument (see Figure S17), the emission of $MPcF_{48}$ is moderately overlapped with the absorption of PTB7-Th, suggesting the presence of energy transfer via Forster resonance energy transfer (FRET).[46] Hence, these results suggest that the subtle change in the metal atom in $MPcF_{48}$ can significantly influence the photophysical and electrochemical properties.

2.2. Photovoltaic Properties. The device performance of binary and ternary OSCs with different fluorinated phthalocyanine small molecules is thoroughly studied. The OSC devices were fabricated with an inverted configuration of ITO/PFN/active layer/V_2O_5/Ag. The ratio of $MPcF_{48}$ in the ternary devices was optimized, as summarized in Tables S1−S3. The ratio of $MPcF_{48}$ to the PTB7-Th:$PC_{70}BM$ blend in the active layer was varied from 0 to 12% while keeping the donor-to-acceptor weight ratio constant at 1:1.5. The binary PTB7-Th:$MPcF_{48}$ blend was performed with a donor-to-acceptor weight ratio of 1:1 for further investigation. The current density versus voltage (*J*−*V*) characteristics of the optimized OSC devices based on the PTB7-Th:$PC_{70}BM$ (1:1.5), PTB7-Th:$PC_{70}BM$:$ZnPcF_{48}$ (1:1.47:0.03), PTB7-Th:$PC_{70}BM$:$CuPcF_{48}$ (1:1.47:0.03), PTB7-Th:$ZnPcF_{48}$ (1:1), and PTB7-Th:$CuPcF_{48}$ (1:1) bulk heterojunction blends under AM 1.5G illumination (100 $mW{\cdot}cm^{-2}$) and dark illumination are shown in Figure 3. The device parameters such as J_{SC}, open-circuit voltage (V_{OC}), fill factor (FF), and PCE are summarized in Table 1. To make a good data statistic, the extracted data were obtained from over 10 devices. As shown in Figure 3a and Table 1, the $PC_{70}BM$-based binary

https://doi.org/10.1021/acsaem.1c00734
ACS Appl. Energy Mater. 2021, 4, 5201−5211

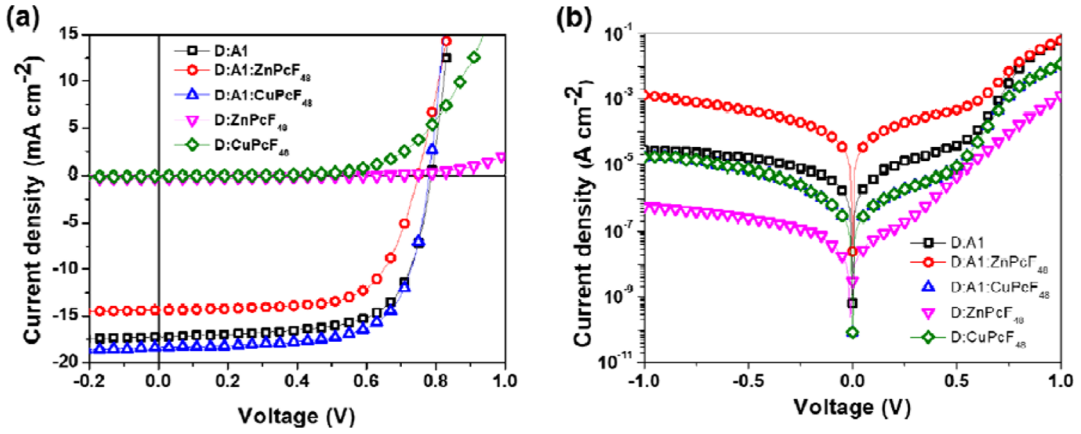

Figure 3. $J-V$ characteristics of the binary and ternary solar cell devices under (a) AM 1.5G illumination and (b) dark condition.

Table 1. Summary of the Device Performance Parameters of Ternary Organic Solar Cells with Different Fluorinated Phthalocyanine Small Molecules[a]

$D:A_1:A_2$	J_{SC} (avg)/$J_{calc.}$[b] [mA·cm^{-2}]	V_{OC} (avg) [V]	FF (avg) [%]	PCE (avg/best) [%]
$D:A_1$	16.82 (16.00)	0.78	68.22	9.01 (9.23)
$D:A_1:ZnPcF_{48}$	14.25 (13.88)	0.77	64.47	7.12 (7.21)
$D:A_1:CuPcF_{48}$	17.90 (17.31)	0.78	68.54	9.57 (9.92)
$D:ZnPcF_{48}$	0.27 (0.25)	0.33	0.50	0.03 (0.07)
$D:CuPcF_{48}$	0.06 (0.06)	0.32	0.24	0.005 (0.006)

[a]Average values were calculated from over 10 devices. [b]$J_{calc.}$ values in parentheses are the integrated current densities calculated from EQE curves.

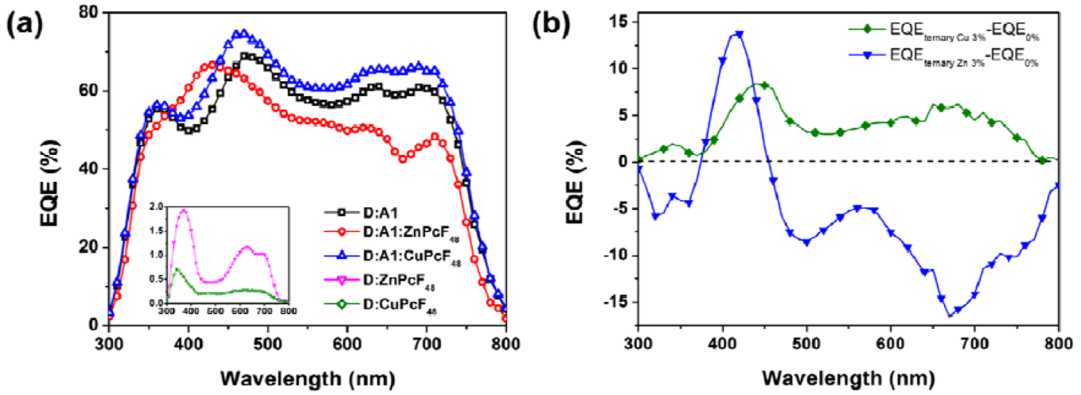

Figure 4. (a) EQE spectra of binary bulk heterojunction OSCs and ternary bulk heterojunction OSCs with two different third components and (b) the ΔEQE values (y-axis) of ternary devices with respect to the $PC_{70}BM$ binary device.

reference OSCs show a max PCE of 9.23% with a J_{SC} of 16.82 mA·cm^{-2}, a V_{OC} of 0.78 V, and a FF of 68.22%. Both $MPcF_{48}$-based binary OSCs show poor device performance compared to $PC_{70}BM$-based binary devices. $CuPcF_{48}$-based binary OSCs show a max PCE of 0.01% with a J_{SC} of 0.06 mA·cm^{-2}, a V_{OC} of 0.32 V, and an FF of 0.24%. Despite having low performance, $ZnPcF_{48}$-based binary OSCs have 1 order of magnitude higher PCE than those of $CuPcF_{48}$-based binary OSCs with a max PCE of 0.07%, a J_{SC} of 0.27 mA·cm^{-2}, a V_{OC} of 0.33 V, and an FF of 0.50%. This may arise from a larger ΔHOMO of PTB7-Th/$ZnPcF_{48}$ (0.54 eV) than that of PTB7-Th/$CuPcF_{48}$ (0.45 eV). As reported by Yang *et al.*, minimizing the energy level offset between a donor and non-fullerene acceptor may provide sufficient driving force for more efficient exciton dissociation, thus increasing the PCE.[47] On the other hand, $ZnPcF_{48}$ TOSCs show a max PCE of 7.21% with a J_{SC} of 14.25 mA·cm^{-2}, a V_{OC} of 0.78 V, and an FF of 64.47%. Even though $ZnPcF_{48}$ exhibits complementary absorption and energy cascade transfer for PTB7-Th and $PC_{70}BM$, its lower device performance than those of $PC_{70}BM$ binary reference devices may be attributed to the tendency of $ZnPcF_{48}$ to solubilize in either the PTB7-Th or $PC_{70}BM$ phase rather than at the PTB7-Th:$PC_{70}BM$ interface.[48] By using contact angle measurement, we found that $ZnPcF_{48}$ materials are likely to be miscible in the acceptor phase (see Table S4). We then explored $CuPcF_{48}$ as the third component in TOSCs. A max PCE of 9.92% with a J_{SC} of 17.90 mA·cm^{-2}, a V_{OC} of 0.78 V, and a FF of 68.54% was achieved. It is demonstrated that their J_{SC} and FF are higher than those of reference binary devices. The enhancement in the J_{SC} is attributed to the complementary absorption profile of the ternary active layer (Figures S14 and S15). A slightly higher value of FF for $CuPcF_{48}$ TOSCs as compared to $PC_{70}BM$ binary OSCs may be related to the fact that $CuPcF_{48}$ improves electron transport.

Figure 3b depicts the $J-V$ characteristic measured in the dark, which gives a further understanding of leakage current

https://doi.org/10.1021/acsaem.1c00734
ACS Appl. Energy Mater. 2021, 4, 5201−5211

and series and shunt resistance in the device performance. The extracted device performance parameters are summarized in Table S5. At the reverse and low forward voltages, the shunt resistance (R_{Sh}) was dominated, which is correlated with the leakage current of the devices. The value of R_{Sh} for $ZnPcF_{48}$ TOSCs is the lowest among other binary TOSCs and $CuPcF_{48}$ TOSCs. As a result, $ZnPcF_{48}$ TOSCs have the highest leakage current, which can dominate the photocurrent and thereby reduce the light current. On the other hand, upon adding $CuPcF_{48}$ in the TOSCs, the leakage current greatly decreases at negative voltages compared to those of binary OSCs. At a region of an applied voltage of around 0.5−1.0 V, $CuPcF_{48}$ TOSCs and $PC_{70}BM$ binary devices have similar series resistance (R_S) values and lower than that of $ZnPcF_{48}$ TOSCs. Similar R_{Sh} values are also observed in $CuPcF_{48}$ TOSCs and $PC_{70}BM$ binary devices, resulting in their similar FF values. A lower FF value of $ZnPcF_{48}$ TOSCs is observed with its much lower R_{Sh} value. It suggests that the parasitic series and shunt resistance effect may contribute to the change of FF in TOSCs.

To gain further insights into enhanced J_{SC} values for $CuPcF_{48}$-based ternary systems, the external quantum efficiency (EQE) spectra were measured, as shown in Figure 4a. Binary PTB7-Th:$PC_{70}BM$, PTB7-Th:$ZnPcF_{48}$, and PTB7-Th:$CuPcF_{48}$ bulk heterojunction solar cells show maximum EQE values of 68.93, 1.93, and 0.71% at wavelengths of 470, 370, and 340 nm, respectively. Meanwhile, the maximum EQE value of 66.68% for $ZnPcF_{48}$ TOSCs is lower than that for binary PTB7-Th:$PC_{70}BM$, and the EQE peak is shifted to a lower wavelength at 430 nm. It indicates that the addition of $ZnPcF_{48}$ as the third component in PTB7-Th:$PC_{70}BM$-based OSCs contributes to the deterioration of the device performance, as shown clearly in Figure 4b, by taking ΔEQE (defined as $EQE_{ternary} - EQE_{binary}$). The contribution of $ZnPcF_{48}$ as the third component in the photon-to-electron conversion capability is can only be seen in a wavelength range of 370−450 nm. On the contrary, $CuPcF_{48}$ TOSCs show an enhanced EQE response in the whole wavelength range of 300−800 nm. The highest value of the EQE response of corresponding $CuPcF_{48}$ TOSCs reaches 74.64% at 470 nm. The escalation of the EQE values for $CuPcF_{48}$ TOSCs together with increased J_{SC} contributes to the FRET effects, which signify that more excitons are generated due to the enhanced absorbed photons in the ternary photoactive layer. These results suggest that the central metal atom substitution in fluorinated phthalocyanines for the third component in TOSCs apparently affects the photon harvesting efficiency. It is worth mentioning that the integrated current densities J_{SC} for binary and ternary devices are in good agreement with the measured J_{SC} values from $J-V$ curves with a maximum error of less than 8%.

The effects of fluorinated zinc and copper phthalocyanines on the charge recombination dynamics were extracted by analyzing V_{OC} and J_{SC} as a function of light intensity (P_{light}). The plot V_{OC} versus the natural logarithm of P_{light} provides information on the degree of trap-assisted recombination under V_{OC} conditions. Typically, a slope (S) equal to 1 kT/q suggests the presence of bimolecular recombination, whereas an S ranging between 1 and 2 ($1\ kT/q \le S \le 2\ kT/q$) indicates the presence of monomolecular recombination and trap-assisted recombination losses.[26,49] Figure 5a shows the plot V_{OC} versus $\ln P_{light}$ for binary devices based on PTB7-Th:$PC_{70}BM$, PTB7-Th:$ZnPcF_{48}$, and PTB7-Th:$CuPcF_{48}$ and ternary OSCs based on PTB7-Th:$PC_{70}BM$:$ZnPcF_{48}$ and

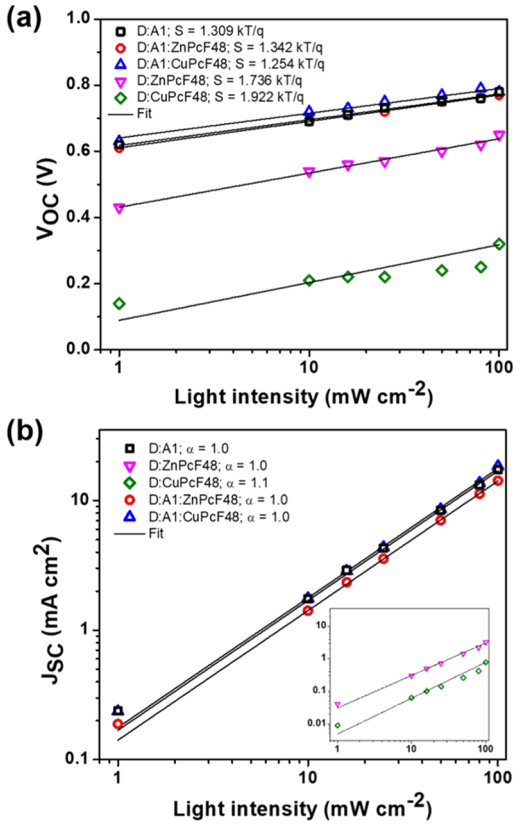

Figure 5. (a) V_{OC} and (b) J_{SC} versus light intensity of binary and ternary films.

PTB7-Th:$PC_{70}BM$:$CuPcF_{48}$. The slope values were calculated to be 1.31 kT/q, 1.74 kT/q, 1.92 kT/q, 1.34 kT/q, and 1.25 kT/q, respectively. These results suggest that the trap-assisted recombination losses can be suppressed by adding a small amount of $CuPcF_{48}$ in TOSCs. Consequently, the J_{SC} and FF of the ternary OSC PTB7-Th:$PC_{70}BM$:$CuPcF_{48}$ simultaneously increase as compared to those of the binary system made of PTB7-Th:$PC_{70}BM$. However, the higher S value of the PTB7-Th:$PC_{70}BM$:$ZnPcF_{48}$ OSC indicates that adding a small concentration of $ZnPcF_{48}$ results in a higher trap-assisted recombination degree, resulting in lower J_{SC} and FF as compared to those of the binary system (see Table 1).

Figure 5b shows the power-law function $J_{SC} \propto P_{light}^{\alpha}$, where α represents the bimolecular recombination intensity. An α value equal to unity ($\alpha = 1$) indicates that bimolecular recombination does not take place within the devices.[50,51] The calculated α values are 1 for all devices, excluding the device PTB7-Th:$CuPcF_{48}$ with $\alpha = 1.1$. The results indicate that there is no bimolecular recombination in all devices.

To gain insights into the influence of zinc and copper phthalocyanines on the charge dynamics, we measured the photocurrent (J_{Ph}) as a function of effective voltage (V_{eff}). J_{Ph} is defined as the difference between the current density measured under 1 sun illumination and that measured under dark conditions ($J_{Ph} = J_L - J_D$). On the other hand, V_{eff} is defined as $V_{eff} = V_0 - V_{app}$, where V_0 is the voltage at $J_{Ph} = 0$ and V_{app} is the applied voltage. Figure 6 shows the J_{Ph} versus V_{eff} plot for the binary OSC based on PTB7-Th:$PC_{70}BM$ and the ternary OSCs PTB7-Th:$PC_{70}BM$:$ZnPcF_{48}$ and PTB7-Th:$PC_{70}BM$:$CuPcF_{48}$. For PTB7-Th:$ZnPcF_{48}$- and PTB7-Th:$CuPcF_{48}$-based devices, the saturation current could not

https://doi.org/10.1021/acsaem.1c00734
ACS Appl. Energy Mater. 2021, 4, 5201−5211

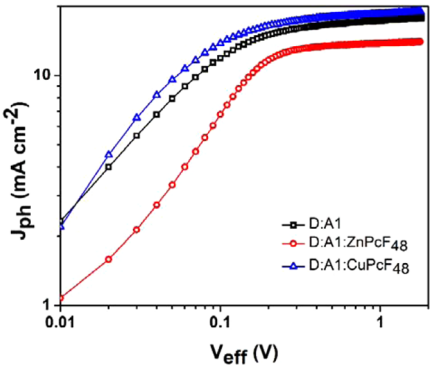

Figure 6. Variation of photocurrent (J_{Ph}) with effective voltage (V_{eff}) in $PC_{70}BM$ binary and ternary solar cell devices.

be reached even at bias >1 V, suggesting severe charge recombination phenomena (see Figures S18–S21). The saturation current density (J_{sat}) is extracted from Figure 3a, where J_{Ph} saturates at a high V_{eff} of over 1.5 V for binary and ternary devices. The maximum charge generation rate (G_{max}) is defined as $J_{sat} = qLG_{max}$, where q is the elementary charge and L is the thickness of the binary or ternary organic layer. Besides, the exciton dissociation efficiency (η_{diss}) is calculated by the J_{Ph}/J_{sat} value under the short-circuit condition, whereas the charge carrier collection efficiency (η_{coll}) is defined by J_{Ph}/J_{sat} under the maximum power point condition. Table S6 summarizes the values of G_{max}, η_{diss}, and η_{coll} for the binary OSC PTB7-Th:$PC_{70}BM$ and the ternary OSCs PTB7-Th:$PC_{70}BM$:$ZnPcF_{48}$ and PTB7-Th:$PC_{70}BM$:$CuPcF_{48}$. In the ternary OSC PTB7-Th:$PC_{70}BM$:$CuPcF_{48}$, G_{max} is slightly higher than those of the binary devices, while the G_{max} of PTB7-Th:$PC_{70}BM$:$ZnPcF_{48}$ is lower than that of the binary system; however, G_{max} for binary–ternary OSCs are almost in the same order of magnitude. Moreover, the PTB7-Th:$PC_{70}BM$:$CuPcF_{48}$ OSC exhibited the highest values of η_{diss} and η_{coll}, indicating that adding 3% $CuPcF_{48}$ into a PTB7-Th:$PC_{70}BM$ system allows improving the charge dynamics of the ternary system. These results agree with the improved J_{SC} and FF of the PTB7-Th:$PC_{70}BM$:$CuPcF_{48}$ OSC in comparison to those of PTB7-Th:$PC_{70}BM$.

2.3. Thin-Film Surface Properties. Even though $ZnPcF_{48}$ and $CuPcF_{48}$ have the same value of the energy band gap ($E_g = E_{HOMO} - E_{LUMO}$) of 1.74 eV and similar HOMO and LUMO values, the $ZnPcF_{48}$-based binary OSC showed an order of magnitude higher efficiency when paired with PTB7-Th than those of $CuPcF_{48}$. The reason behind this may correlate with the different morphology of the bulk film, as shown in Figure 7. The tapping mode atomic force microscopy (AFM) measurements were performed to investigate the bulk surface morphology changes by introducing $MPcF_{48}$ to the PTB7-Th:$PC_{70}BM$-blend system. The corresponding AFM height and phase images for the PTB7-Th:$MPcF_{48}$ blend are shown in Figure 7a,b (the top part is two-dimensional images, the middle part is three-dimensional images, and the bottom part is the phase images). Both $MPcF_{48}$-based binary blends show a coarse, distinctive phase-separated morphology with a large island-like domain. Larger domain sizes on the photoactive layer of OSCs are not favorable for charge transport or exciton diffusion, thus explaining why $MPcF_{48}$ binary OSCs have inferior device performance (see Table 1). Even though both $MPcF_{48}$ binary blends have a large domain and very rough

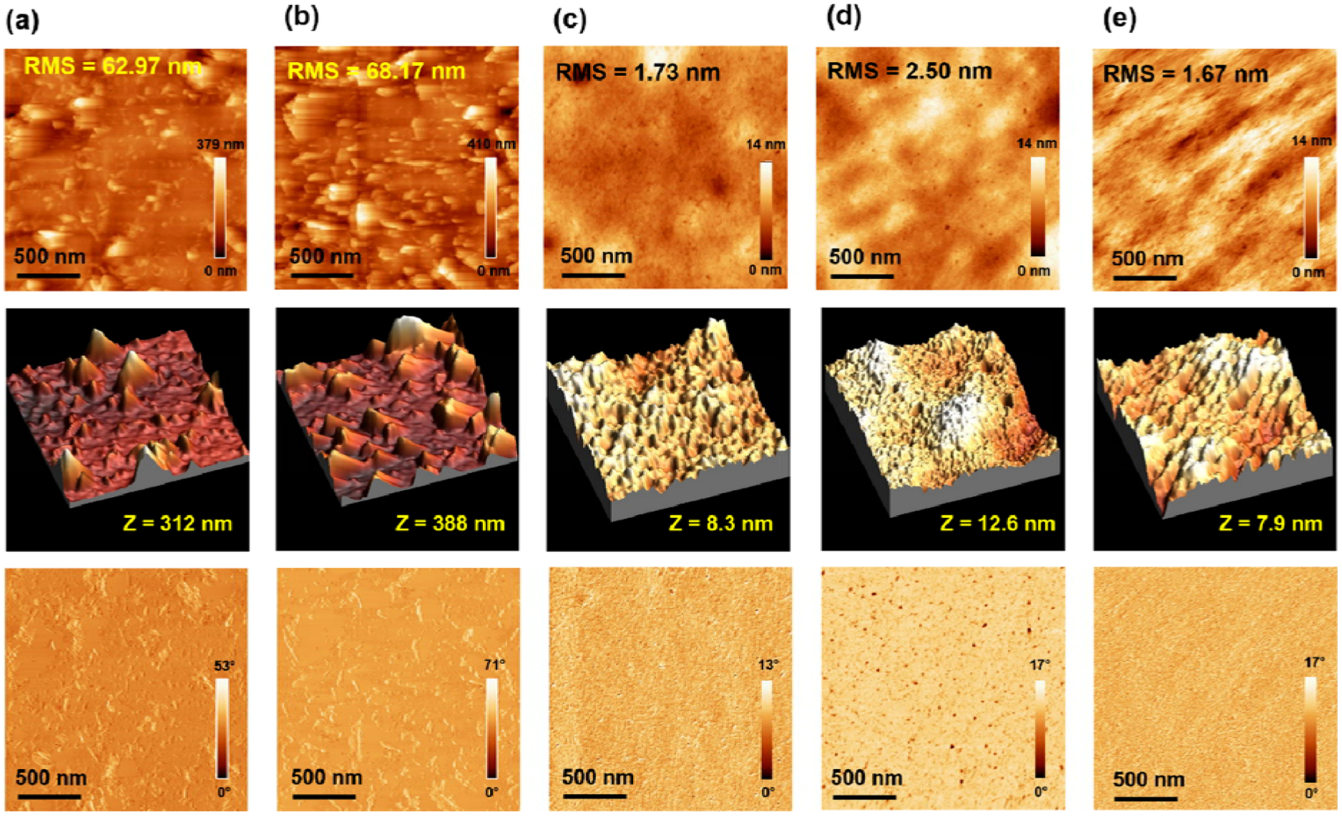

Figure 7. AFM height images (top), AFM three-dimensional height images (middle), and AFM phase images (bottom) ($2 \times 2\ \mu m^2$) of binary (a) D:$ZnPcF_{48}$, (b) D:$CuPcF_{48}$, and (c) D:A_1 and ternary (d) D:A_1:$ZnPcF_{48}$ and (e) D:A_1:$CuPcF_{48}$.

https://doi.org/10.1021/acsaem.1c00734
ACS Appl. Energy Mater. 2021, 4, 5201–5211

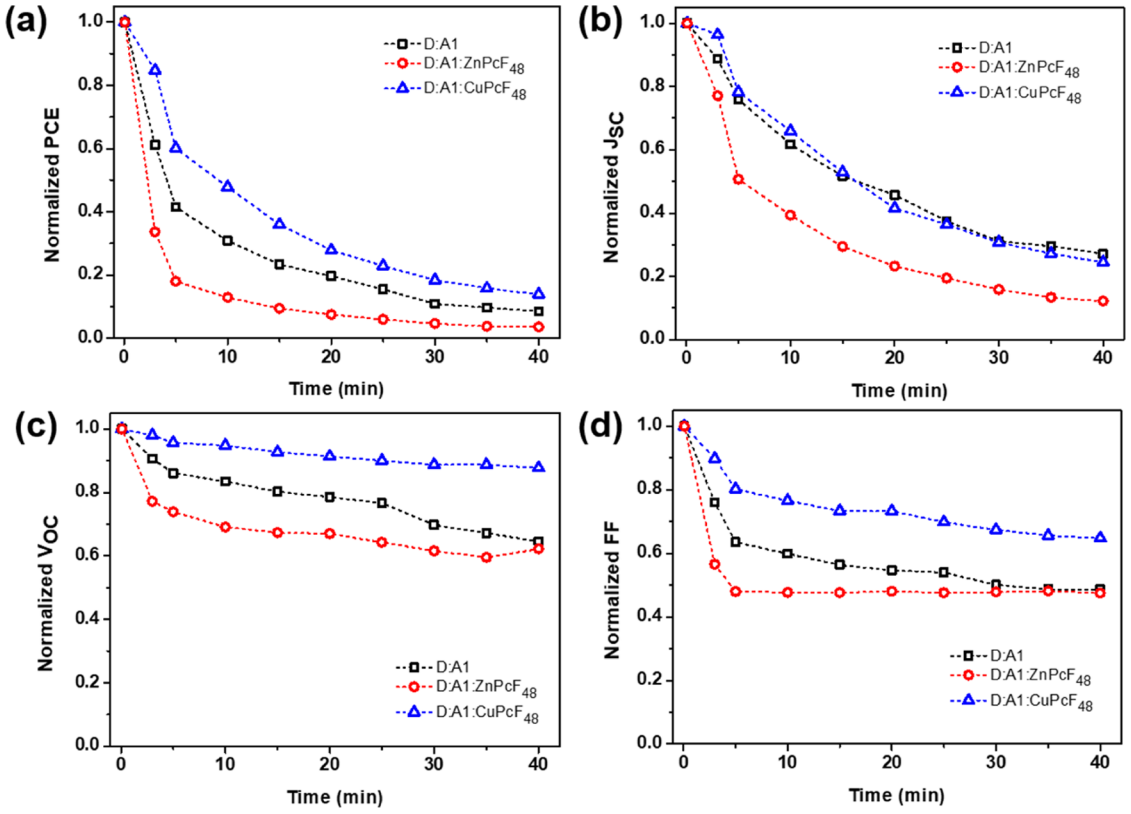

Figure 8. Normalized (a) PCE, (b) J_{SC}, (c) V_{OC}, and (d) FF of $PC_{70}BM$ binary, $ZnPcF_{48}$ ternary, and $CuPcF_{48}$ ternary devices over photoaging time.

surfaces, the $ZnPcF_{48}$-based binary blend shows clearly less aggregation because ZnPcs are known to disperse better in solution than CuPcs.[52] Compared to the PTB7-Th:$CuPcF_{48}$ blend, the PTB7-Th:$ZnPcF_{48}$ blend shows a lower root-mean-square (RMS) roughness of ~63 nm, less aggregation with smaller hills, and a smaller height difference, as shown in its corresponding 3D height and phase images. This result is in good agreement with the higher performance of the $ZnPcF_{48}$-based binary OSC than the $CuPcF_{48}$-based binary OSC. Due to the poor morphology of the $MPcF_{48}$ binary film, they are likely to play a bigger role than small energetic differences.

Figure 7c displays the morphology of the binary reference PTB7-Th:$PC_{70}BM$ blend film featuring a smooth crystallized-like domain with an RMS roughness of 1.72 nm. In the case of a ternary system, the addition of 3% $ZnPcF_{48}$ as the third component in the PTB7-Th:$PC_{70}BM$ blend results in an increased RMS roughness of 2.5 nm and a larger height difference of 12.6 nm, as shown in Figure 7d. Moreover, the formation of the homogeneous dispersity of pinholes on the $ZnPcF_{48}$ ternary blend film is clearly observed in the phase image, which is not beneficial to facilitate charge transport. On the other hand, the incorporation of 3% $CuPcF_{48}$ in the PTB7-Th:$PC_{70}BM$ blend effectively decreases RMS to 1.67 nm and results in a finer interpenetrating bulk heterojunction morphology relative to the $PC_{70}BM$-binary blend, as shown in Figure 7e. The smoother morphology of the PTB7-Th:$PC_{70}BM$:$CuPcF_{48}$ ternary blend compared to the $PC_{70}BM$ binary blend may explain the reduced recombination losses and better charge dynamics of $CuPcF_{48}$-based ternary blend compared to the binary blend, which has been reflected in the higher values of FF and J_{SC} in the incorporation of $CuPcF_{48}$ as the third component in TOSC devices.

2.4. Stability Study. In addition to high device performance, the information about ambient stability is necessarily important for the future commercialization of OSCs. Generally, the ambient photostability of OSCs depends on several factors, such as exposure to humidity and oxygen, intrinsic properties of the organic materials, fullerene dimerization in FA-based OSCs, microstructural stability of NFA-based OSCs, etc. Recent studies about the photostability investigation of ternary OSCs showed that the incorporation of the third component might enhance the photostability of the ternary system by minimizing the molecular structural changes, preserving the crystallinity, deactivating the light-induced trap formation, and balancing the charge carrier mobilities in their active layers upon photodegradation exposure.[53,54] We believe that the incorporation of $MPcF_{48}$ as the third component in TOSCs may affect the device photostability. Thus, we performed the photostability study of nonencapsulated binary and ternary devices exposed under continuous AM 1.5G illumination at the open-circuit condition in an ambient atmosphere (room temperature and relative humidity = 50–60%).

The evolution results of photovoltaic parameters for all devices under the ambient photodegradation test are presented in Figure 8. $ZnPcF_{48}$ TOSCs suffer the most in degradation with more than 95% efficiency loss after 40 min of illumination, as shown in Figure 8a. On the other hand, the PCE of $PC_{70}BM$ binary OSCs is reduced by 90% from its original value. The most stable device is $CuPcF_{48}$ TOSCs, with a PCE decay of almost 85%. Reasonable photoaging decay was noticed for all photovoltaic parameters in all devices, as shown in Figure 8b–d. It is obvious to see that J_{SC} decay in all photodegraded devices has similar behavior with PCE decay

https://doi.org/10.1021/acsaem.1c00734
ACS Appl. Energy Mater. 2021, 4, 5201–5211

behavior, suggesting that J_{SC} is the main contributor to the observed PCE loss. Moreover, it is observed that FF decay also contributes to the PCE loss after J_{SC} decay. A relatively higher J_{SC} and FF loss in photodegraded $ZnPcF_{48}$ TOSCs may be attributed to the morphological instabilities of bulk heterojunction.[55] On the other hand, the addition of 3% $CuPcF_{48}$ in the binary PTB7-Th:$PC_{70}BM$ blend can moderately enhance the ambient photostability, verified by the relatively lowest V_{OC} and FF loss. This result indicates that the metal atom substitution strategy in the third component of TOSCs affects the photostability of OSCs. Further study needs to be carefully carried out to go more in depth into the main degradation mechanism caused by the metal atom substitution of $MPcF_{48}$ as the third component in TOSCs for a full application of the ternary strategy in the future.

3. CONCLUSIONS

In summary, we have successfully synthesized fluorinated zinc and copper phthalocyanines ($ZnPcF_{48}$ and $CuPcF_{48}$) as new third components in ternary OSCs with a device architecture of ITO/PFN/PTB7-Th:$PC_{70}BM$:$MPcF_{48}$/V_2O_5/Ag. The introduction of $MPcF_{48}$ with different central atoms has an influence on the electronic structure, optical absorption, energy level alignment, charge transport and recombination, and blend film morphology of TOSCs. Among $MPcF_{48}$ derivatives, $CuPcF_{48}$ has the highest PCE of up to 9.92%, due to its better morphology, improved exciton dissociation, better charge carrier collection efficiency, and more suppressed trap-assisted recombination, thus making it a promising new NFA material for OSC applications. Further studies are in progress to optimize the devices using new CuPcs as the third component of TOSCs to increase PV performance and stability.

4. EXPERIMENTAL METHOD

4.1. Materials. An indium tin oxide (ITO)-patterned glass substrate with a resistivity of 10 $\Omega \cdot sq^{-1}$ was purchased from PsiOTec Ltd. Poly[(9,9-bis(3′-(*N*,*N*-dimethylamino)propyl)-2,7-fluorene)-*alt*-2,7-(9,9-dioctylfluorene)] (PFN) and vanadium oxide (V_2O_5) as electron and hole transport layer materials were obtained from 1-Material Inc. and Sigma-Aldrich, respectively. Active layer materials used were based on the polymer donor poly[4,8-bis(5-(2-ethylhexyl)-thiophen-2-yl)benzo[1,2-b;4,5-b′]dithiophene-2,6-diyl-*alt*-(4-(2-ethylhexyl)-3-fluorothieno[3,4-*b*]-thiophene)-2-carboxylate-2,6-diyl] (PTB7-Th) and the fullerene acceptor [6,6]-phenyl-C_{70}-butyric acid methyl ester ($PC_{70}BM$), which were purchased from 1-Material Inc. The third components of the non-fullerene acceptors of zinc- and copper-fluorinated phthalocyanines were synthesized. The chemical structure of active materials in the ternary system is shown in Figure 1. High-purity silver (Ag) was purchased from Testbourne Ltd. All solvents were used as received unless otherwise noted.

4.2. Synthesis of 3,6-Difluoro-4,5-bis(pentafluorophenoxy)-phthalonitrile 1. Tetrafluorophthalonitrile (2.0 g, 10 mmol), pentafluorophenol (3.7 g, 20 mmol), and KF (4.0 g, 69 mmol) were dissolved in 20 mL of acetone under an inert atmosphere and stirring at room temperature for 3 days. The solution was filtered, dried under $MgSO_4$, filtered again, and concentrated under vacuum. The white solid was washed with methanol yielding 3.0 g (57%) of 3,6-difluoro-4,5-bis(pentafluorophenoxy)phthalonitrile **1**. ^{13}C NMR (75 MHz, $CDCl_3$): δ = 152.0 (dd, J = 265, 3.9 Hz), 142.5−138.9 (m), 141.6−141.2 (m), 140.0−136.0, 138.0−137.0 (m), 130.3−130.0 (m), 108.6, 102.3−101.9 (m). MS-MALDI-TOF m/z: 527.872. ν_{max}(KBr)/cm^{-1}: 2247 (C≡N), 1520, 1478, 1397, 1315, 1287, 1164, 1119, 1089, 999. mp = 120 °C.

4.3. Synthesis of $ZnPcF_{48}$. Phthalonitrile **1** (300 mg, 0.66 mmol) and $Zn(OAc)_2$ (208 mg, 1.14 mmol) were added in a pressure tube and heated at 160 °C overnight. The blue mixture was cooled to room temperature and purified by column chromatography (DCM), yielding 35 mg (11%) of $ZnPcF_{48}$. ^{19}F NMR (300 MHz, THF-d_8): δ = −134.8 (s), −157.9 (d, J = 23 Hz), −162.5 (t, J = 23 Hz), −164.50 (t, J = 22 Hz). ^{13}C NMR (125 MHz, THF-d_8): δ = 150.5 (s), 148.1−146.0 (dd, J = 266, 4 Hz), 143.1−141.1 (dd, J = 252, 11 Hz), 140.9−138.7 (m), 140.2−139.9 (m), 139.9−138.0 (m), 132.8 (m), 122.6 (m). ^{13}C {^{19}F} NMR (125 MHz, THF-d_8): δ = 150.5, 147.1, 142.1, 139.9, 139.8, 139.1, 132.8, 122.6. UV−vis ($CHCl_3$) λ_{max}/nm (log ε): 365 (4.75), 625 (4.54), 664 (4.62), 694 (5.32). HR-MALDI-TOF (dithranol) m/z for $C_{80}F_{48}N_8O_8Zn$: calcd, 2175.8359; found, 2175.8419. ν_{max}(KBr)/cm^{-1}: 1520, 1476, 1417, 1322, 1167, 1122, 1002.

4.4. Synthesis of $CuPcF_{48}$. Phthalonitrile **1** (300 mg, 0.66 mmol) and $CuCl_2$ (76 mg, 0.66 mmol) were added in a pressure tube and heated at 160 °C overnight. The blue mixture was cooled to room temperature, dissolved in DCM, filtered, and concentrated under vacuum. The green solid was washed with MeOH and purified by Soxhlet extraction using THF obtaining $CuPcF_{48}$ (105 mg, 34%). UV−vis ($CHCl_3$) λ_{max}/nm (log ε): 355 (4.73), 625 (4.50), 664 (4.42), 697 (5.20). HR-MALDI-TOF (dithranol) m/z for $C_{80}CuF_{48}N_8O_8$: calcd, 2174.8441; found, 2174.8420. ν_{max}(KBr)/cm^{-1}: 1520, 1478, 1420, 1321, 1257, 1268, 1125, 1001.

4.5. Device Fabrication. The reported OSC devices were fabricated using an inverted structure of ITO/PFN/PTB7-Th:$PC_{70}BM$:$MPcF_{48}$/V_2O_5/Ag. The ITO-coated glass substrate was cleaned with a surface-active cleaning agent and diluted in deionized water. The substrate was sonicated in acetone, methanol, and isopropanol anhydrous solvents for 10 min subsequently. The cleaned substrate was dried at 120 °C in an oven for 20 min and transferred to a UV/ozone cleaner for 15 min. PFN as an electron transport layer was dissolved in methanol with the presence of a small amount of acetic acid (2 $\mu L \cdot mL^{-1}$). The PFN solution with a concentration of 2 $mg \cdot mL^{-1}$ was spin-coated on the cleaned substrate to obtain a 10 nm thickness. The active layer blend solution was prepared by dissolving the donor and acceptor materials in chlorobenzene and 1,8-diiodooctane (97:3% v/v) with a final concentration of 25 $mg \cdot mL^{-1}$. The weight ratio of donor/fullerene acceptor/metallophthalocyanines was 1:1.5-*x*:*x*. The blend solution was stirred and heated at 40 °C overnight, followed by solution aging for 48 h. After the aging time, the blend solution was spin-coated on top of the interlayer at 750 rpm for 30 s to obtain a 100 nm thickness of the active layer. Afterward, the anode layer consisting of 3 nm of V_2O_5 and 100 nm of Ag was deposited by thermal evaporation under high vacuum conditions ($\lesssim 1 \times 10^{-6}$ mbar) with an evaporation rate of 0.01 $nm \cdot s^{-1}$. The effective area for all devices was 0.09 cm^2. The device optimization results are shown in Tables S1−S3.

4.6. Characterization. UV−vis spectra were recorded using a Helios Gamma spectrophotometer. ^{13}C NMR spectra were recorded at 25 °C using Bruker AC300 and Bruker AC500 spectrometers. For ^{19}F spectra, trifluorotoluene served as an external standard (δ = −63.9 ppm). High-resolution mass spectra were obtained from a Bruker Microflex LRF20 matrix-assisted laser desorption/ionization time-of-flight (MALDI-TOF) using dithranol as a matrix. Differential pulse voltammetry was performed in a conventional three-electrode cell using a μ-AUTOLAB type III potentiostat/galvanostat at a scan rate of 100 $mV \cdot s^{-1}$. A platinum working electrode, a Ag/$AgNO_3$ reference electrode, and a platinum wire counter electrode were employed. Ferrocene/ferrocenium was used as an internal standard for all measurements. Photoluminescence measurements were performed on a fluorescence spectrophotometer from Photon Technology International Inc. (Birmingham, NJ) with a Xe lamp used as the excitation light source at room temperature and an excitation wavelength of 610 nm. The electrical properties of OSC devices (J−V characteristics) were determined using a solar simulator (Abet Technologies model 11000 class type A, Xenon arc) and a Keithley 2400 Source Measure Unit under illumination and dark conditions in the forward voltage sweep direction from −1 to 1 V. The light intensity was calibrated by an NREL certified monocrystalline silicon photodiode. The external quantum efficiency (EQE) measurements were carried out in the

https://doi.org/10.1021/acsaem.1c00734
ACS Appl. Energy Mater. 2021, 4, 5201−5211

forward wavelength sweep direction from 300 to 800 nm using a Lasing IPCE-DC model with a series number of LS1109-232. The film morphologies were studied by AFM using silicon probes with a spring constant of 5 $N \cdot m^{-1}$ in a tapping mode with a resonant frequency of 150 kHz and a tip radius of 1 nm.

■ ASSOCIATED CONTENT

Supporting Information

The Supporting Information is available free of charge at https://pubs.acs.org/doi/10.1021/acsaem.1c00734.

NMR spectra; FT-IR spectra; MS-MALDI-TOF; HR-MALDI-TOF; UV−vis spectra of thin-film blends; photoluminescence spectrum; electrochemical characterization; device optimization; and characterization (PDF)

■ AUTHOR INFORMATION

Corresponding Authors

Josep Pallarès − *Department of Electric, Electronic and Automatic Engineering, Universitat Rovira i Virgili, Tarragona 43007, Spain;* orcid.org/0000-0001-7221-5383; Email: josep.pallares@urv.cat

Ángela Sastre-Santos − *Área de Química Orgánica, Instituto de Bioingeniería, Universidad Miguel Hernández de Elche, Elche 03202, Spain;* orcid.org/0000-0002-8835-2486; Email: asastre@umh.es

Lluis F. Marsal − *Department of Electric, Electronic and Automatic Engineering, Universitat Rovira i Virgili, Tarragona 43007, Spain;* orcid.org/0000-0002-5976-1408; Email: lluis.marsal@urv.cat

Authors

Alfonsina Abat Amelenan Torimtubun − *Department of Electric, Electronic and Automatic Engineering, Universitat Rovira i Virgili, Tarragona 43007, Spain*

Jorge Follana-Berná − *Área de Química Orgánica, Instituto de Bioingeniería, Universidad Miguel Hernández de Elche, Elche 03202, Spain*

José G. Sánchez − *Department of Electric, Electronic and Automatic Engineering, Universitat Rovira i Virgili, Tarragona 43007, Spain*

Complete contact information is available at: https://pubs.acs.org/10.1021/acsaem.1c00734

Author Contributions

A.S.-S. and J.F.-B. designed and synthesized $MPcF_{48}$. L.F.M., J.P., A.A.A.T., and J.G.S. fabricated and characterized the solar cells. The manuscript was written through contributions of all authors. All authors have given approval to the final version of the manuscript.

Notes

The authors declare no competing financial interest.

■ ACKNOWLEDGMENTS

This work was financially supported by the European Regional Development Fund "A way to make Europe" and the Spanish Ministerio de Ciencia e Innovacion Agencia Estatal de Investigación (grant number CTQ2017-87102-R AEI/FEDER UE) and by the European Union's Horizon 2020 research and innovation program under the Marie Skłodowska-Curie (grant agreement number 713679) and was partially supported by the Spanish Ministerio de Ciencia, Innovación y Universidades (MICINN/FEDER) (grant number RTI2018-094040-B-I00), by the Agency for Management of University and Research Grants (AGAUR) (grant agreement ref 2017-SGR-1527), and by the Catalan Institution for Research and Advanced Studies (ICREA) under the ICREA Academia Award.

■ DEDICATION

Dedicated to Prof. Tomás Torres on the occasion of his 70th birthday

■ REFERENCES

(1) He, Z.; Xiao, B.; Liu, F.; Wu, H.; Yang, Y.; Xiao, S.; Wang, C.; Russell, T. P.; Cao, Y. Single-Junction Polymer Solar Cells with High Efficiency and Photovoltage. *Nat. Photonics* **2015**, *9*, 174−179.

(2) Shen, P.; Yao, M.; Wang, G.; Mi, R.; Guo, W.; Bai, Y.; Shen, L. High-Efficiency Polymer Solar Cells with Low Temperature Solution-Processed SnO2/PFN as a Dual-Function Electron Transporting Layer. *J. Mater. Chem. A* **2018**, *6*, 17401−17408.

(3) Sánchez, J. G.; Balderrama, V. S.; Garduño, S. I.; Osorio, E.; Viterisi, A.; Estrada, M.; Ferré-Borrull, J.; Pallarès, J.; Marsal, L. F. Impact of Inkjet Printed ZnO Electron Transport Layer on the Characteristics of Polymer Solar Cells. *RSC Adv.* **2018**, *8*, 13094−13102.

(4) Zhao, B.; He, Z.; Cheng, X.; Qin, D.; Yun, M.; Wang, M.; Huang, X.; Wu, J.; Wu, H.; Cao, Y. Flexible Polymer Solar Cells with Power Conversion Efficiency of 8.7%. *J. Mater. Chem. C* **2014**, *2*, 5077−5082.

(5) Bihar, E.; Corzo, D.; Hidalgo, T. C.; Rosas-Villalva, D.; Salama, K. N.; Inal, S.; Baran, D. Fully Inkjet-Printed, Ultrathin and Conformable Organic Photovoltaics as Power Source Based on Cross-Linked PEDOT:PSS Electrodes. *Adv. Mater. Technol.* **2020**, *5*, No. 2000226.

(6) Liu, Y.; Qi, N.; Song, T.; Jia, M.; Xia, Z.; Yuan, Z.; Yuan, W.; Zhang, K.-Q.; Sun, B. Highly Flexible and Lightweight Organic Solar Cells on Biocompatible Silk Fibroin. *ACS Appl. Mater. Interfaces* **2014**, *6*, 20670−20675.

(7) Liu, Q.; Jiang, Y.; Jin, K.; Qin, J.; Xu, J.; Li, W.; Xiong, J.; Liu, J.; Xiao, Z.; Sun, K.; Yang, S.; Zhang, X.; Ding, L. 18% Efficiency Organic Solar Cells. *Sci. Bull.* **2020**, *65*, 272−275.

(8) Meng, L.; Zhang, Y.; Wan, X.; Li, C.; Zhang, X.; Wang, Y.; Ke, X.; Xiao, Z.; Ding, L.; Xia, R.; Yip, H. L.; Cao, Y.; Chen, Y. Organic and Solution-Processed Tandem Solar Cells with 17.3% Efficiency. *Science* **2018**, *361*, 1094−1098.

(9) Torimtubun, A. A. A.; Sánchez, J. G.; Pallarès, J.; Marsal, L. F. A Cathode Interface Engineering Approach for the Comprehensive Study of Indoor Performance Enhancement in Organic Photovoltaics. *Sustainable Energy Fuels* **2020**, *4*, 3378−3387.

(10) Balderrama, V. S.; Sánchez, J. G.; Lastra, G.; Cambarau, W.; Arias, S.; Pallarès, J.; Palomares, E.; Estrada, M.; Marsal, L. F. High-Efficiency Organic Solar Cells Based on a Halide Salt and Polyfluorene Polymer with a High Alignment-Level of the Cathode Selective Contact. *J. Mater. Chem. A* **2018**, *6*, 22534−22544.

(11) Jiang, W.; Yu, R.; Liu, Z.; Peng, R.; Mi, D.; Hong, L.; Wei, Q.; Hou, J.; Kuang, Y.; Ge, Z. Ternary Nonfullerene Polymer Solar Cells with 12.16% Efficiency by Introducing One Acceptor with Cascading Energy Level and Complementary Absorption. *Adv. Mater.* **2018**, *30*, No. 1703005.

(12) Salim, M. B.; Nekovei, R.; Jeyakumar, R. Organic Tandem Solar Cells with 18.6% Efficiency. *Sol. Energy* **2020**, *198*, 160−166.

(13) Firdaus, Y.; He, Q.; Lin, Y.; Nugroho, F. A. A.; Le Corre, V. M.; Yengel, E.; Balawi, A. H.; Seitkhan, A.; Laquai, F.; Langhammer, C.; Liu, F.; Heeney, M.; Anthopoulos, T. D. Novel Wide-Bandgap Non-Fullerene Acceptors for Efficient Tandem Organic Solar Cells. *J. Mater. Chem. A* **2020**, *8*, 1164−1175.

(14) Shi, Z.; Bai, Y.; Chen, X.; Zeng, R.; Tan, Z. Tandem Structure: A Breakthrough in Power Conversion Efficiency for Highly Efficient Polymer Solar Cells. *Sustainable Energy Fuels* **2019**, *3*, 910−934.

(15) Weng, K.; Li, C.; Bi, P.; Ryu, H. S.; Guo, Y.; Hao, X.; Zhao, D.; Li, W.; Woo, H. Y.; Sun, Y. Ternary Organic Solar Cells Based on Two Compatible PDI-Based Acceptors with an Enhanced Power Conversion Efficiency. *J. Mater. Chem. A* **2019**, *7*, 3552−3557.
(16) An, Q.; Zhang, F.; Zhang, J.; Tang, W.; Deng, Z.; Hu, B. Versatile Ternary Organic Solar Cells: A Critical Review Energy & Environmental Science a Critical Review. *Energy Environ. Sci.* **2016**, *9*, 281−322.
(17) Gasparini, N.; Salleo, A.; Mcculloch, I.; Baran, D. The Role of the Third Component in Ternary Organic Solar Cells. *Nat. Rev. Mater.* **2019**, *4*, 229−242.
(18) Bi, P.; Hao, X. Versatile Ternary Approach for Novel Organic Solar Cells: A Review. *Sol. RRL* **2019**, *3*, No. 1800263.
(19) Liu, X.; Yan, Y.; Yao, Y.; Liang, Z. Ternary Blend Strategy for Achieving High-Efficiency Organic Solar Cells with Nonfullerene Acceptors Involved. *Adv. Funct. Mater.* **2018**, *28*, No. 1802004.
(20) Lakhotiya, G.; Belsare, N.; Arbuj, S.; Kale, B.; Rana, A. Enhanced Performance of PTB7-Th: PCBM Based Active Layers in Ternary Organic Solar Cells. *RSC Adv.* **2019**, *9*, 7457−7463.
(21) Zhan, L.; Li, S.; Lau, T.; Cui, Y.; Lu, X.; Shi, M.; Li, C.; Li, H.; Hou, J.; Chen, H. Over 17% Efficiency Ternary Organic Solar Cells Enabled by Two Non-Fullerene Acceptors Working in an Alloy-like Model. *Energy Environ. Sci.* **2020**, *13*, 635−645.
(22) Cheng, P.; Wang, J.; Zhang, Q.; Huang, W.; Zhu, J.; Wang, R.; Chang, S. Y.; Sun, P.; Meng, L.; Zhao, H.; Cheng, H. W.; Huang, T.; Liu, Y.; Wang, C.; Zhu, C.; You, W.; Zhan, X.; Yang, Y. Unique Energy Alignments of a Ternary Material System toward High-Performance Organic Photovoltaics. *Adv. Mater.* **2018**, *30*, No. 1801501.
(23) Lin, Y. C.; Cheng, H. W.; Su, Y. W.; Lin, B. H.; Lu, Y. J.; Chen, C. H.; Chen, H. C.; Yang, Y.; Wei, K. H. Molecular Engineering of Side Chain Architecture of Conjugated Polymers Enhances Performance of Photovoltaics by Tuning Ternary Blend Structures. *Nano Energy* **2018**, *43*, 138−148.
(24) Cheng, H.-W.; Zhang, H.; Lin, Y.-C.; She, N.-Z.; Wang, R.; Chen, C.-H.; Yuan, J.; Tsao, C.-S.; Yabushita, A.; Zou, Y.; Gao, F.; Cheng, P.; Wei, K.-H.; Yang, Y. Realizing Efficient Charge/Energy Transfer and Charge Extraction in Fullerene-Free Organic Photovoltaics via a Versatile Third Component. *Nano Lett.* **2019**, *19*, 5053−5061.
(25) Yang, C.; Sun, Y.; Li, Q.; Liu, K.; Xue, X.; Huang, Y.; Ren, K.; Li, L.; Chen, Y.; Wang, Z.; Qu, S.; Wang, Z. Nonfullerene Ternary Organic Solar Cell with Effective Charge Transfer between Two Acceptors. *J. Phys. Chem. Lett.* **2020**, *11*, 927−934.
(26) Xiao, L.; He, B.; Xiao, L.; He, B.; Hu, Q.; Maserati, L.; Zhao, Y.; Yang, B.; Kolaczkowski, M. A.; Anderson, C. L.; Borys, N. J.; Klivansky, L. M.; Chen, T. L.; Schwartzberg, A. M.; Russell, T. P.; Cao, Y.; Peng, X.; et al. Multiple Roles of a Non-Fullerene Acceptor Contribute Synergistically for High-Efficiency Ternary Organic Photovoltaics Multiple Roles of a Non-Fullerene Acceptor Contribute Synergistically for High-Efficiency Ternary Organic Photovoltaics. *Joule* **2018**, *2*, 2154−2166.
(27) Zhang, J.; Tan, H. S.; Guo, X.; Facchetti, A.; Yan, H. Material Insights and Challenges for Non-Fullerene Organic Solar Cells Based on Small Molecular Acceptors. *Nat. Energy* **2018**, *3*, 720−731.
(28) Cui, Y.; Yao, H.; Zhang, J.; Zhang, T.; Wang, Y.; Hong, L.; Xian, K.; Xu, B.; Zhang, S.; Peng, J.; Wei, Z.; Gao, F.; Hou, J. Over 16% Efficiency Organic Photovoltaic Cells Enabled by a Chlorinated Acceptor with Increased Open-Circuit Voltages. *Nat. Commun.* **2019**, *10*, No. 2515.
(29) Stenta, C.; Molina, D.; Viterisi, A.; Montero-Rama, M. P.; Pla, S.; Cambarau, W.; Fernández-Lázaro, F.; Palomares, E.; Marsal, L. F.; Sastre-Santos, Á. Diphenylphenoxy-Thiophene-PDI Dimers as Acceptors for OPV Applications with Open Circuit Voltage Approaching 1 Volt. *Nanomaterials* **2018**, *8*, No. 211.
(30) Krishnan Jagadamma, L.; Sajjad, M. T.; Savikhin, V.; Toney, M. F.; Samuel, I. D. W. Correlating Photovoltaic Properties of a PTB7-Th:PC71BM Blend to Photophysics and Microstructure as a Function of Thermal Annealing. *J. Mater. Chem. A* **2017**, *5*, 14646−14657.
(31) Sanchez, J. G.; Torimtubun, A. A. A.; Balderrama, V. S.; Estrada, M.; Pallares, J.; Marsal, L. F. Effects of Annealing Temperature on the Performance of Organic Solar Cells Based on Polymer: Non-Fullerene Using V2O5 as HTL. *IEEE J. Electron Devices Soc.* **2020**, *8*, 421−428.
(32) Martín-Gomis, L.; Fernández-Lázaro, F.; Sastre-Santos, Á. Advances in Phthalocyanine-Sensitized Solar Cells (PcSSCs). *J. Mater. Chem. A* **2014**, *2*, 15672−15682.
(33) Urbani, M.; De La Torre, G.; Nazeeruddin, M. K.; Torres, T. Phthalocyanines and Porphyrinoid Analogues as Hole-and Electron-Transporting Materials for Perovskite Solar Cells. *Chem. Soc. Rev.* **2019**, *48*, 2738−2766.
(34) Urbani, M.; Ragoussi, M. E.; Nazeeruddin, M. K.; Torres, T. Phthalocyanines for Dye-Sensitized Solar Cells. *Coord. Chem. Rev.* **2019**, *381*, 1−64.
(35) Molina, D.; Guerrero, A.; Garcia-Belmonte, G.; Fernández-Lázaro, F.; Sastre-Santos, Á. Synthesis of a Fully Conjugated Phthalocyanine-Diketopyrrolopyrrole- Phthalocyanine Triad as Low Band Gap Donor in Small Molecule Bulk Heterojunction Solar Cells. *Eur. J. Org. Chem.* **2014**, *2014*, 4585−4591.
(36) Wang, Y.; Zhuang, C.; Fang, Y.; Yu, H.; Wang, B. Various Roles of Dye Molecules in Organic Ternary Blend Solar Cells. *Dyes Pigm.* **2020**, *176*, No. 108231.
(37) Faure, M. D. M.; Grant, T. M.; Lessard, B. H. Silicon Phthalocyanines as Acceptor Candidates in Mixed Solution/Evaporation Processed Planar Heterojunction Organic Photovoltaic Devices. *Coatings* **2019**, *9*, No. 203.
(38) Honda, S.; Nogami, T.; Ohkita, H.; Benten, H.; Ito, S. Improvement of the Light-Harvesting Efficiency in Polymer/Fullerene Bulk Heterojunction Solar Cells by Interfacial Dye Modification. *ACS Appl. Mater. Interfaces* **2009**, *1*, 804−810.
(39) Honda, S.; Yokoya, S.; Ohkita, H.; Benten, H.; Ito, S. Light-Harvesting Mechanism in Polymer/Fullerene/Dye Ternary Blends Studied by Transient Absorption Spectroscopy. *J. Phys. Chem. C* **2011**, *115*, 11306−11317.
(40) Xu, H.; Ohkita, H.; Tamai, Y.; Benten, H.; Ito, S. Interface Engineering for Ternary Blend Polymer Solar Cells with a Heterostructured Near-IR Dye. *Adv. Mater.* **2015**, *27*, 5868−5874.
(41) Ke, L.; Min, J.; Adam, M.; Gasparini, N.; Hou, Y.; Perea, J. D.; Chen, W.; Zhang, H.; Fladischer, S.; Sale, A. C.; Spiecker, E.; Tykwinski, R. R.; Brabec, C. J.; Ameri, T. A Series of Pyrene-Substituted Silicon Phthalocyanines as Near-IR Sensitizers in Organic Ternary Solar Cells. *Adv. Energy Mater.* **2016**, *6*, No. 1502355.
(42) Vebber, M. C.; Grant, T. M.; Brusso, J. L.; Lessard, B. H. Bis(Trialkylsilyl Oxide) Silicon Phthalocyanines: Understanding the Role of Solubility in Device Performance as Ternary Additives in Organic Photovoltaics. *Langmuir* **2020**, *36*, 2612−2621.
(43) Xu, Z. X.; Roy, V. A. L.; Low, K. H.; Che, C. M. Bulk Heterojunction Photovoltaic Cells Based on Tetra-Methyl Substituted Copper(Ii) Phthalocyanine:P3HT:PCBM Composite. *Chem. Commun.* **2011**, *47*, 9654−9656.
(44) Stylianakis, M. M.; Konios, D.; Viskadouros, G.; Vernardou, D.; Katsarakis, N.; Koudoumas, E.; Anastasiadis, S. H.; Stratakis, E.; Kymakis, E. Ternary Organic Solar Cells Incorporating Zinc Phthalocyanine with Improved Performance Exceeding 8.5%. *Dyes Pigm.* **2017**, *146*, 408−413.
(45) Huang, H.; Li, X.; Chen, S.; Qiu, B.; Du, J.; Meng, L.; Zhang, Z.; Yang, C.; Li, Y. Enhanced Performance of Ternary Organic Solar Cells with a Wide Bandgap Acceptor as the Third Component. *J. Mater. Chem. A* **2019**, *7*, 27423−27431.
(46) Bi, P.; Zheng, F.; Yang, X.; Niu, M.; Feng, L.; Qin, W.; Hao, X. Dual Forster Resonance Energy Transfer Effects in Non-Fullerene Ternary Organic Solar Cells with the Third Component Embedded in the Donor and Acceptor. *J. Mater. Chem. A* **2017**, *5*, 12120−12130.
(47) Yang, C.; Zhang, J.; Liang, N.; Yao, H.; Wei, Z.; He, C.; Yuan, X.; Hou, J. Effects of Energy-Level Offset between a Donor and Acceptor on the Photovoltaic Performance of Non-Fullerene Organic Solar Cells. *J. Mater. Chem. A* **2019**, *7*, 18889−18897.

https://doi.org/10.1021/acsaem.1c00734
ACS Appl. Energy Mater. 2021, 4, 5201−5211

(48) Lessard, B. H.; Dang, J. D.; Grant, T. M.; Gao, D.; Seferos, D. S.; Bender, T. P. Bis(Tri-n-hexylsilyl Oxide) Silicon Phthalocyanine: A Unique Additive in Ternary Bulk Heterojunction Organic Photovoltaic Devices. *ACS Appl. Mater. Interfaces* **2014**, *6*, 15040−15051.
(49) Kirchartz, T.; Nelson, J. Meaning of Reaction Orders in Polymer:Fullerene Solar Cells. *Phys. Rev. B* **2012**, *86*, No. 165201.
(50) Koster, L. J. A.; Kemerink, M.; Wienk, M. M.; Maturová, K.; Janssen, R. A. J. Quantifying Bimolecular Recombination Losses in Organic Bulk Heterojunction Solar Cells. *Adv. Mater.* **2011**, *23*, 1670−1674.
(51) Lakhwani, G.; Rao, A.; Friend, R. H. Bimolecular Recombination in Organic Photovoltaics. *Annu. Rev. Phys. Chem.* **2014**, *65*, 557−581.
(52) Ito, M.; Palanisamy, K.; Kumar, A.; Murugesan, V. S.; Shin, P. K.; Tsuda, N.; Yamada, J.; Ochiai, S. Characterization of the Organic Thin Film Solar Cells with Active Layers of PTB7/PC71BM Prepared by Using Solvent Mixtures with Different Additives. *Int. J. Photoenergy* **2014**, *2014*, 1−8.
(53) Doumon, N. Y.; Houard, F. V.; Dong, J.; Christodoulis, P.; Dryzhov, M. V.; Portale, G.; Koster, L. J. A. Improved Photostability in Ternary Blend Organic Solar Cells: The Role of [70]PCBM. *J. Mater. Chem. C* **2019**, *7*, 5104−5111.
(54) Gasparini, N.; Paleti, S. H. K.; Bertrandie, J.; Cai, G.; Zhang, G.; Wadsworth, A.; Lu, X.; Yip, H. L.; Mcculloch, I.; Baran, D. Exploiting Ternary Blends for Improved Photostability in High-Efficiency Organic Solar Cells. *ACS Energy Lett.* **2020**, *5*, 1371−1379.
(55) Zhang, K. N.; Jiang, Z. N.; Wang, T.; Niu, M. S.; Feng, L.; Qin, C. C.; So, S. K.; Hao, X. T. High-Performance Ternary Organic Solar Cells with Morphology-Modulated Hole Transfer and Improved Ultraviolet Photostability. *Sol. RRL* **2020**, No. 2000165.

https://doi.org/10.1021/acsaem.1c00734
ACS Appl. Energy Mater. 2021, 4, 5201−5211